J. Fluid Mech. (1999), *vol.* 398, *pp.* 155–180. Printed in the United Kingdom

Buoyancy-driven mean flow in a long channel with a hydraulically constrained exit condition

By TH. GRIMM AND T. MAXWORTHY

Department of Aerospace and Mechanical Engineering, University of Southern California, Los Angeles, CA 90089-1191, USA

(Received 11 August 1998 and in revised form 7 May 1999)

Convection plays a major role in a variety of natural hydrodynamic systems. Those in which convection drives exchange flows through a lateral contraction and/or over a sill form a special class with typical examples being the Red and Mediterranean Seas, the Persian Gulf, and the fjords that indent many coastlines. The present work focuses on the spatial distribution and scaling of the density difference between the inflowing and outflowing fluid layers. Using a long water-filled channel, fitted with buoyancy sources at its upper surface, experiments were conducted to investigate the influence of the geometry of the strait and the channel as well as the magnitude of the buoyancy flux. Two different scaling laws, one by Phillips (1966), and one by Maxworthy (1994, 1997) were compared with the experimental results. It has been shown that a scaling law for which $g' = k\,B_0^{2/3}x/h^{4/3}$ best describes the distribution of the observed density difference along the channel, where B_0 is the buoyancy flux, x the distance from the closed end of the channel, h its height at the open end (sill) and k a constant that depends on the details of the channel geometry and flow conditions. This result holds for the experimental results and appears to be valid for a number of natural systems as well.

1. Introduction

In partially enclosed water bodies like the Red and Mediterranean Seas, the fjords that indent many coastlines, etc., the mean fluid motion is driven by buoyancy differences that are induced by convective motion. Usually a rather small strait connects the open ocean to the partially enclosed sea. Due to the generally observed density difference between the two water bodies an exchange flow is established through the strait. Within the partially enclosed body of fluid a continuous buoyancy flux replenishes the exchange flow through the strait. This buoyancy flux can be due to evaporation, cooling or freezing at the surface. The magnitude of the buoyancy flux is, in general, difficult to calculate. Also a wide variety of natural causes can disturb the system, for example strong surface winds or localized cooling or heating.

In laboratory experiments, on the other hand, it is rather easy to control the geometry and the buoyancy forcing of the experimental apparatus and change many of the parameters at will. Here we report on experiments in a channel that was built to study such flows. A better understanding is sought of the combined effect of the buoyancy forcing, the geometry of the enclosed water body itself and the geometry of the sea strait on the flow pattern inside the channel and through the strait. The results from the experiments are then compared with natural systems.

First the literature of this problem is reviewed along with the underlying theory.

Following this, the experimental apparatus is presented, the experimental procedures and the results of the experiments are discussed; finally comparisons are made with natural systems.

1.1. *Literature*

In general the literature concerning the subject presented in this work can be divided into two groups: on one hand, publications that deal with the circulation and motion of the fluid in the partially enclosed water body itself; on the other, questions that arise concerning the controlling mechanisms of the connecting strait between two reservoirs of different fluid densities.

The seminal work on convection and circulation in partially enclosed water bodies was published by Phillips (1966). Here basic expressions were found for the velocity and buoyancy distribution, and the results were compared with field data from the Red Sea, collected by Neumann & McGill (1961). This model will be discussed more thoroughly in the next section. Refinements of the Phillips' model were presented by Garrett, Speer & Tragou (1995) and Tragou & Garrett (1995), for example, by incorporating viscous and conductive effects. Some experimental studies were also conducted also Brocard, Jirka & Harleman (1977)

The influence of a strait on flows of this type was investigated by Stommel & Farmer (1953). Here for the first time the expression *overmixed* was used for an exchange flow through a strait when a minimum density difference existed between the fluid layers in the strait while the exchange flow through the strait was maximal. In this state additional mixing inside the reservoir had no further effect on lowering the density difference or increasing the amount of exchanged fluid. A more complete discussion of this flow state will be found in § 2.1.1. Theoretical studies of the effects of straits were performed by Armi (1986), Farmer & Armi (1986), Armi & Farmer (1986) and compared with the flow through the Strait of Gibraltar. Different strait geometries were considered, for example lateral contractions with and without a sill and the effect of a barotropic net flux through the strait. A good review can be found in Lawrence (1990), where the different methods of defining critical flow conditions are discussed and related to one another.

A first attempt to inter-relate the flows in the region of convectively driven mean flows (called the channel in what follows) and the specifics of the flow through the strait is to be found in Maxworthy (1994, 1997). Here the relationship between the buoyancy and interfacial forces acting on the fluid body in the enclosed reservoir and the control state of the flow through the strait was considered. This model is fundamental to the present work and will be discussed in depth in the following section. Based on this approach experiments were carried out by Grimm & Maxworthy (1996) and Grimm (1998). In these works it was first shown that a theory that combines the flow properties in the strait with those in the channel can describe the types of flows investigated in experiments and seems to be valid for a number of natural systems as well.

2. Remarks on the underlying theory

2.1. *Critical flow condition*

Throughout this work the concept of an internally hydraulically critical flow is fundamental, especially in the application to two-layer flows, which are usually observed in sea straits or estuaries where two reservoirs of different fluid densities are connected. The flow is critical, in a continuous transition from subcritical to

supercritical conditions, at the location where the area is a minimum, and the local Froude number (see below) is unity, cf. the concept of a critical Mach number in gas dynamics. An introduction to this concept can be found in Henderson (1966), for example.

Further hydraulic assumptions must be made for the flows considered here. These assumptions are that the fluid is considered to be inviscid, the pressure hydrostatic everywhere in the flow and the velocity and density of each layer constant at a fixed axial location, x. Changes of these properties only take place in the direction of the flow. Additionally the flow is assumed to be Boussinesq, meaning changes in density are only considered in calculating buoyancy effects.

In order to determine the location where the flow becomes critical, a suitable Froude number must be calculated, and the flow is considered to be critical when this Froude number is unity. For two-layer flows a composite Froude number, usually designated as G, is the appropriate quantity to consider. This is derived from the Froude numbers, Fr_i, of each individual fluid layer, where

$$Fr_i^2 = \frac{u_i^2}{g' y_i}; \tag{2.1}$$

here u_i is the fluid velocity in the x-direction in the strait, y_i is the layer thickness there, and g' is the reduced gravity based on the density difference between the layers, so that $g' = g(\rho_2 - \rho_1)/\rho_2$, where the indexes 1 and 2 represent the upper and lower fluid layer respectively, g is the gravitational constant and ρ_i is the density of each fluid layer (see figure 1). Then the composite Froude number is given by

$$G^2 = Fr_1^2 + Fr_2^2 - (1 - r)\, Fr_1^2 Fr_2^2, \tag{2.2}$$

with $r = \rho_1/\rho_2$. Since a small density difference is assumed the last term in (2.2) vanishes and the composite Froude number becomes

$$G^2 = Fr_1^2 + Fr_2^2. \tag{2.3}$$

A value $G^2 > 1$ represents supercritical conditions and the flow is subject to upstream control. On the other hand, if $G^2 < 1$, the flow is subcritical and subject to downstream control. A supercritical flow is connected to subcritical conditions by a hydraulic jump in the absence of a geometric control. Good reviews of the subject can be found in Armi (1986), Farmer & Armi (1986), Armi & Farmer (1986), Lawrence (1990), and Williams & Armi (1991).

2.1.1. *Basic equations and extensions to the concept of hydraulic control*

If critical flow conditions are caused by a contraction in either or both the lateral and vertical directions, the flow is called hydraulically controlled. For all the experiments discussed in what follows, the cross-section of the contraction is rectangular and the shallowest and narrowest sections coincide, and the internal Froude number is unity at that location.

For the cases considered here in which the density differences are caused by a surface buoyancy flux (B_0) the conservation of volume and buoyancy, are given by (see Maxworthy 1997)

$$(1 - \alpha)u_1 = -\alpha u_2, \tag{2.4}$$

$$B_0 LW = \alpha h g' u_2, \tag{2.5}$$

independent of the amount of mixing that occurs in the channel, where B_0 is the buoyancy flux, L is the length of the channel, W is the ratio between the width of

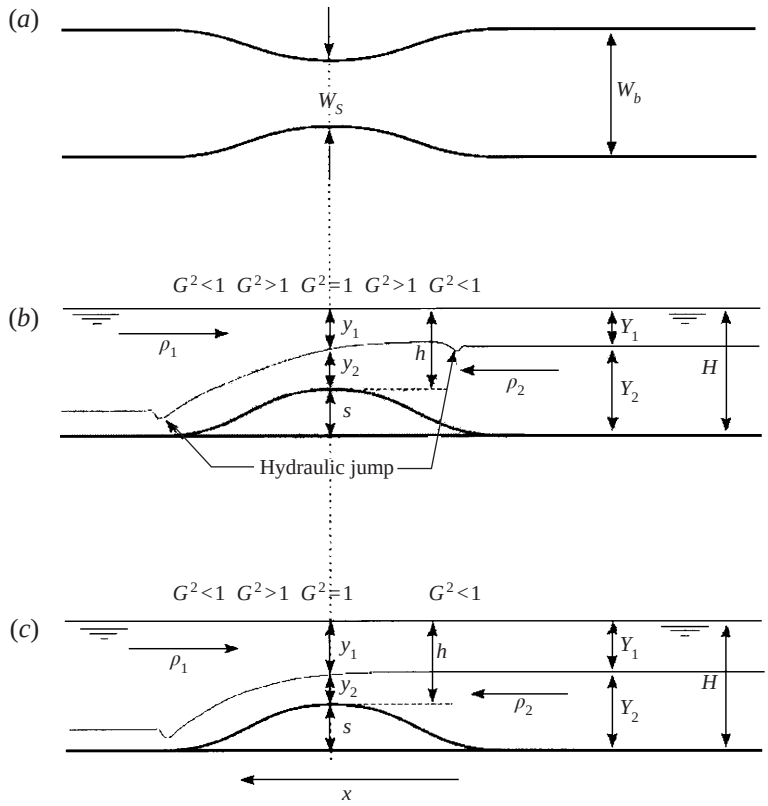

FIGURE 1. Schematic view of the contraction region. (*a*) View of the contraction region from the top. (*b*) Side view with complete flow isolation by two supercritical flow regions on either side of the channel (*limiting control* (*overmixed*)). (*c*) Side view of the control region with separation of the flow field only on one side of the contraction (*basic hydraulic control*).

the basin, W_b, and the width of the sill, W_S, in the narrowest part of the contraction, h is the total fluid depth at the sill and $y_2 = \alpha h$ the thickness of the lower fluid layer at that location. Other quantities of interest are shown in figure 1.

With $G^2 = 1$ and using (2.4) and (2.5) we obtain for the dimensionless buoyancy difference (F), volume flux (Q) and kinetic energy (K)

$$\frac{g'h}{(B_0LW)^{2/3}} = \frac{1}{\alpha}\left(1 + \frac{\alpha^3}{(1-\alpha)^3}\right)^{1/3} = F(\alpha), \tag{2.6}$$

$$\frac{u_2 \alpha h W_s}{(B_0L)^{1/3} W_B h} = \frac{1}{W^{2/3}F(\alpha)} = Q(\alpha; W), \tag{2.7}$$

$$\frac{u_1^2 + u_2^2}{2(B_0L)^{2/3}} = \frac{W^{2/3}E(\alpha)}{2F(\alpha)} = K(\alpha; W), \tag{2.8}$$

where $E(\alpha) = [1/\alpha^2 + 1/(1-\alpha)^2]$. Both functions $E(\alpha)$ and $F(\alpha)$ have minima, of 8 and $4^{2/3} = 2.52$ respectively, at $\alpha = 0.5$, no matter how the contraction is formed, and become infinite as α approaches 0 or 1. The minimum state is critical to the discussion that follows since it represents the limiting condition on the flow that can occur at the strait/sill location. We start the discussion of this state by evaluating equations

(2.6) to (2.8) at $\alpha = 0.5$ which give, for this limiting control condition,

$$g' = (4B_0LW)^{2/3}/h, \tag{2.9}$$

$$Q = 1/(4W)^{2/3}, \tag{2.10}$$

$$K = (4W^2)^{1/3}, \tag{2.11}$$

so that g' and K are at a minimum and Q at a maximum independent of how much mixing takes place in the channel.

Thus, as will be seen, for a hydraulically controlled two-layer flow through a contraction two cases have to be considered. In the first the hydraulic control condition is satisfied at the shallowest and narrowest section, but only on one side of the contraction is the flow hydraulically separated from the flow in the contraction by a supercritical flow region; see figure 1*c*). This case will be termed *basic control*. The second case entails a control with supercritical flow regions on both sides of the contraction. Due to these supercritical flow regions the flow through the sill does not depend on the conditions in the two connecting reservoirs (figure 1*b*).

A variation of the latter case was first investigated by Stommel & Farmer (1953) who studied the influence of a contraction on the amount of mixing that can occur in an estuary. Here for the first time the expression *overmixed* was used for an exchange flow through a strait marked by a minimum in the density difference between the fluid layers, while the volumetric exchange of fluid through the strait was at a maximum and its kinetic energy a minimum, independent of the reservoir conditions. Note that this is identical to the state described by equations (2.9) to (2.11) in the present case. Also, as mentioned above, in order for the flow to be in this state, the control conditions in the strait region had to be such that no information concerning the reservoir conditions could travel across the strait in either direction. This meant that if, by some arbitrary mixing mechanism, the density difference in one of the reservoirs could have been reduced to a very small value, or even disappeared completely, no effect of this mixing would have been observed in the flow through the strait itself, hence the use of the term overmixed. The major shortcoming of this term is that it is used to descibe a flow state which is set, primarily, by a control at the strait while the word itself suggests the importance of an effect which is actually secondary, the amount of mixing in the reservoir. Since, in what follows, we use the term *basic control* for a flow which is controlled at the strait, but not to the extend described above, the term *limiting control* is used which more accurately conveys the concept of the limiting control condition that is attained as α reaches a value of $\frac{1}{2}$. Further discussion of these different flow states will be found in the following sections when the results of our experiments are presented.

2.2. *Scaling laws for the density differences in the main channel and control section*

The earliest attempt to study the scaling relationships for density difference and velocity in the main channel was contained in the seminal publication of Phillips (1966). Subsequently this theory was refined by other authors, e.g. Garrett *et al.* (1995) or Tragou & Garrett (1995). However all of these authors ignored the hydraulic condition at the strait which resulted in some conclusions that appear to contradict existing observations. It is required that vertical mixing be active over the whole depth and length, and that the local Froude number be constant along the whole length of the channel. The necessary hydraulic constraints were included in a unified approach by Maxworthy (1994, 1997).

2.2.1. *The Phillips (1966) scaling*

The approach by Phillips (1966) was to scale the density difference between the upper and lower layers in a channel flow based on similarity arguments that resulted in functional forms for the distributions of the flow properties like velocity and buoyancy. These similarity functions for the velocity u and and g' have the following form:

$$u_{sim} = (B_0 x)^{1/3} f_1\left(\frac{y}{z}\right), \tag{2.12}$$

$$g'_{sim} = \frac{(B_0 x)^{2/3}}{z} f_2\left(\frac{y}{z}\right), \tag{2.13}$$

where the f_i are universal non-dimensional functions describing the vertical profile of u_{sim} and g'_{sim}, and z is the local fluid depth. The important conclusion to be drawn from these equations is that the horizontal velocity component, u_{sim}, of the flow at a specific scaled height y/z is proportional to $(B_0 x)^{1/3}$ and is independent of the depth z. The density difference or g'_{sim} is proportional to $(B_0 x)^{2/3} z^{-1}$ for a given scaled depth y/z. The dependency of g' on x, z and B_0 is the same as in (2.6), with $W = 1$, if x is replaced by the total length L of the channel and the local depth z by h, but clearly neither the change in channel width nor the control state of the flow in the strait was taken into account. If a local Richardson number is formed based on (2.12) and (2.13) it is found that $Ri = g' z\, u^{-2} = f_2/f_1^2 = \text{const.}$

2.2.2. *The frictional approach of Maxworthy*

In more recent publications Maxworthy (1994, 1997) has put forward a different formulation. Here the hydraulic exit conditions were explicitly taken into account, as will be discussed in the next section, while the body of the fluid in the main channel was taken to be in buoyancy–friction balance as in Maxworthy & Monismith (1988). The resulting scaling based on that balance can be expressed as follows:

$$g'_{Ma} = \mathscr{K} \frac{(B_0 L)^{2/3}}{\mathscr{H}} \left(\frac{L}{\mathscr{H}}\right)^{1/3} \equiv \mathscr{K} \frac{B_0^{2/3} L}{\mathscr{H}^{4/3}}, \tag{2.14}$$

where $\mathscr{K}$ is a proportionality factor, yet to be determined, which accounts for the geometry of the channel and the hydraulic state in the strait, and $\mathscr{H}$ is the combined thickness of the two moving fluid layers in the channel, which, in general, is not the total depth H of the channel. Critically, the same scaling can be found using a different argument. If we assume that no mixing takes place between the two layers, as found experimentally, then a local buoyancy flux balance, similar to that of equation (2.5), gives $g' \sim x$. The only possible combination of B_0, h or $\mathscr{H}$ and x or L that gives this result is equations (2.14) and (2.15). Note, the important difference compared with Phillips' (1966) (2.13) is the inclusion of the multiplying factor of $(L/\mathscr{H})^{1/3}$. Due to this factor g'_{Ma} scales linearly with the longitudinal direction and the power of $\mathscr{H}$ becomes $-4/3$.

2.2.3. *Scaling based on hydraulic control in the strait*

In the original formulation of the scaling law (2.14) the total length L of the channel was used. Since in the context of this paper the buoyancy distribution along the longitudinal axis of the channel is of interest, a function $g'(x)$ is introduced, where the local variable x is used instead of L. Furthermore from the experiments and also from field data it was noted that $\mathscr{H}$ is usually of the order of h, meaning that only a small amount of fluid from below the level of the sill crest is lifted up to exit over

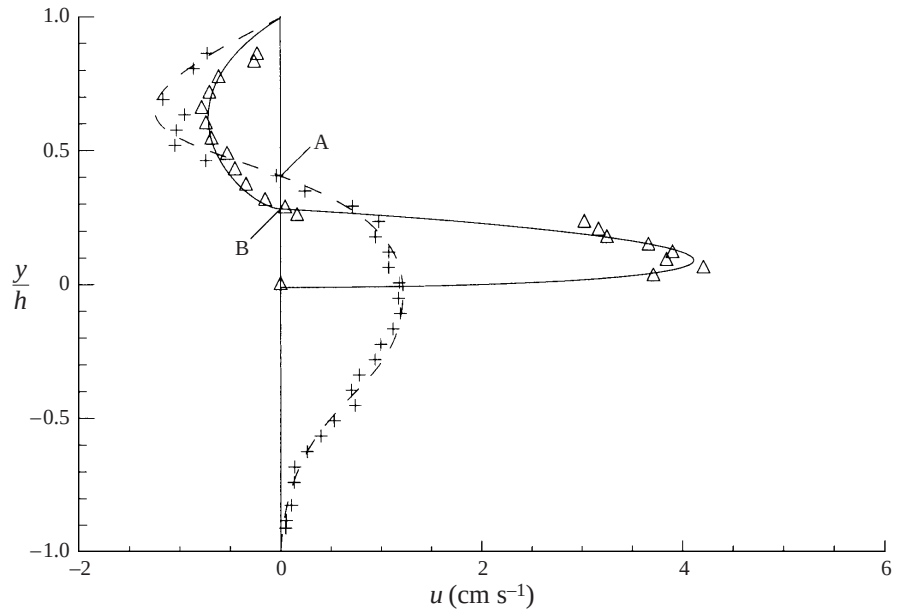

FIGURE 2. Example of a velocity profile in the contraction region. The △ represent the profile directly on top of the sill crest. The + represent a cross-section some 16 cm towards the closed end of the channel. Almost no fluid motion is observed below $y/h = 0.5$. Note the drop of the interface from inside the channel (β_S) (point A) to a lower position at the sill crest (α) (point B) (experimental conditions: $\lambda = 50$, $W = 1$, $B_0 = 0.12\,\mathrm{cm^2\,s^{-3}}$).

the sill and through the contraction. An example of this effect in the experiments is shown in figure 2. The velocity profile furthest from the sill crest (+) goes to zero before it reaches the bottom of the channel and one can estimate that the effective depth of this layer is of order $-0.3h$.

Therefore, when $\mathscr{H}$ is replaced by h, i.e. only true independent variables are used, an equation of the following form is obtained:

$$g'(x) = k\frac{(B_0 x)^{2/3}}{h}\left(\frac{x}{h}\right)^{1/3} = k\frac{B_0^{2/3}x}{h^{4/3}}, \tag{2.15}$$

where k is a proportionality factor. For the controlled state of the flow, equation (2.6) must still hold while from equation (2.15) a value of $g'(L)$ for the full length of the channel can be derived. Equating these two expressions for g' gives

$$F(\alpha)\,\frac{(B_0 L W)^{2/3}}{h} = k\frac{B_0^{2/3}L}{h^{4/3}}. \tag{2.16}$$

This equation can be solved for k to give

$$k = F(\alpha)\,W^{2/3}\left(\frac{h}{L}\right)^{1/3}. \tag{2.17}$$

Combining (2.15) and (2.17) results in a scaling function for $g'(x)$ for a two-layer flow over a sill and through a contraction, with a hydraulic constraint at the narrowest and shallowest location of the following form:

$$g'(x) = F(\alpha)\,W^{2/3}\lambda^{-1/3}\,\frac{B_0^{2/3}x}{h^{4/3}}, \tag{2.18}$$

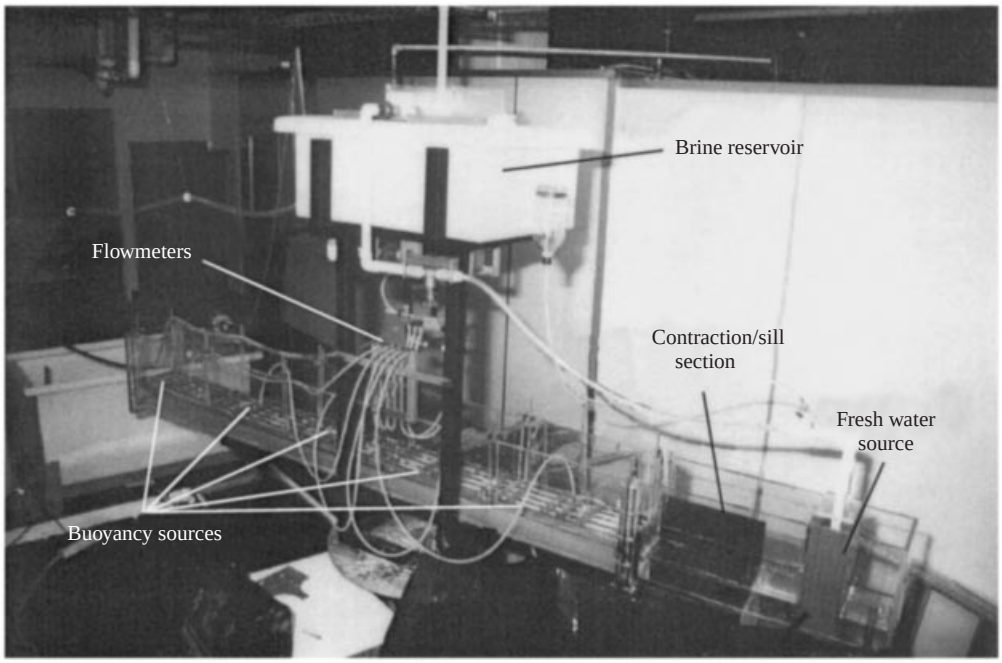

FIGURE 3. Photograph of the experimental setup.

where $\lambda = L/h$. Compared with the former scaling functions this latter one requires the knowledge of an additional parameter, the non-dimensional interface depth α at the sill. Later in the results section it is shown that (2.18) can be simplified further if the control state (basic or limiting control (overmixed)) is known.

3. Experimental apparatus

The main part of the apparatus consisted of a long channel, 300 cm long, 20.5 cm wide and 30 cm deep, made from Acrylic plastic. In order to simulate the buoyancy flux due to evaporation, surface freezing or cooling, a saturated brine solution was evenly applied, at a measured flow rate, to the surface of the upper layer through porous buoyancy sources (figures 3 and 4). Fresh water was added at one side of the tank, which will be called the 'open end' or 'open reservoir' in what follows. The other, longer, side of the channel, which was covered by the buoyancy sources, was closed, hence it will be called the 'closed end' or 'closed channel'. The two ends of the tank were separated by a region into which contractions and sills of various forms could be placed. The open end of the channel simulated the open ocean. The closed end represented a partially enclosed sea like the Red or Mediterranean Seas. The contraction or sill region represents the strait between the open and the closed ends.

Two dependent variables, velocity and density, were measured. Velocity profiles were mainly taken in the sill region using a DPIV method. Density profiles were obtained by slowly sucking water from the channel using thin flexible tubes at various locations and depths along its length. This fluid was passed through a conductivity probe, where its conductivity, C, was measured continuously to an accuracy of 0.5% ($C < 20\,000$ μS) and 1% ($C < 200\,000$ μS). A calibration function was used to

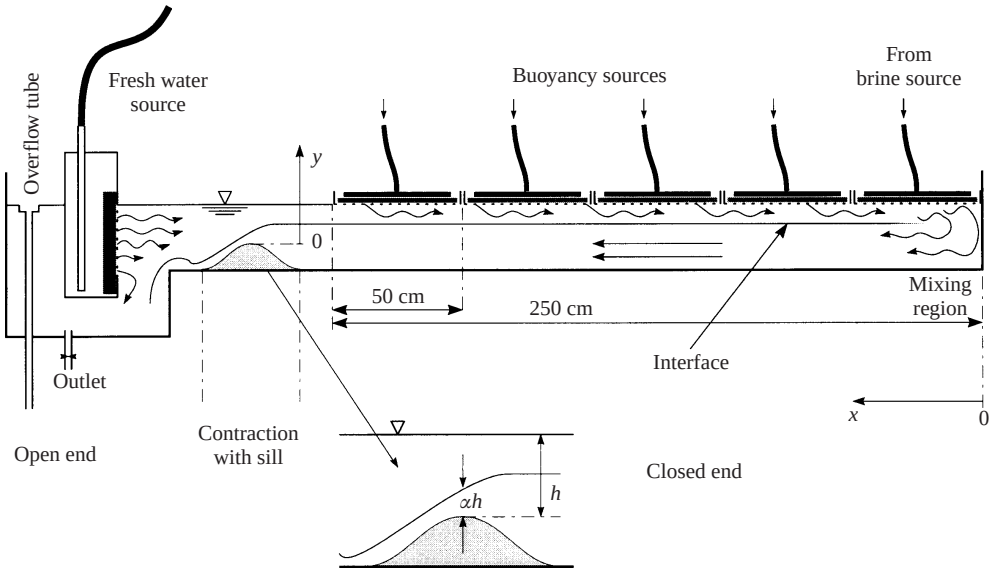

FIGURE 4. Schematic view of the channel and the buoyancy sources.

translate the conductivity values into density with an accuracy of about ± 0.00025 g cm^{-3}.

The following subsections describe the different sections of the channel and the methods by which the data were obtained. For a more detailed description of the experimental setup see Grimm (1998). Figure 3 shows a photograph of the setup and figure 4 a sketch.

3.1. *The channel*

3.1.1. *The closed end and the buoyancy sources*

As described above, the channel was divided into three different sections. The open end, the sill or contraction region and the closed-end. The closed end had a variable length (50–250 cm) and was completely covered by five buoyancy sources each 50 cm long. The sources were individually controlled which allowed for time-dependent or spatially varying buoyancy forcing. The frames of the buoyancy sources were built from stainless steel with a fine screen at the bottom, which supported two layers of filter paper with a thick, foam-like material in between. This allows the brine to be distributed very evenly before it flows into the water underneath the sources. Brine was supplied from an overflow basin through valves, flow meters and drip tubes that eventually fed the sources (see figure 4).

3.1.2. *The sill/contraction region*

The sill and/or contraction region of the channel separated the open and the closed end. Lateral and vertical (sill) contractions were inserted so that the narrowest and the shallowest sections always coincided if they were used simultaneously. The contour of each contraction was sinusoidal in shape, when used separately. However, in cases where the lateral and vertical contractions were used together, the vertical contraction (sill) had a rectangular cross-section and was placed between the sinusoidally shaped lateral contractions at their narrowest point. The resulting cross-section of the contraction was always rectangular. A comparison of results for a sinusoidally

shaped sill versus a rectangularly shaped one revealed no significant changes in the flow field with respect to the maximum density difference and the velocity field in the contraction region. Using a rectangular bar rather than a more gently varying sinusoidally shaped sill conflicts with the assumption that pressure is hydrostatic everywhere in the flow. However, it was also shown by Henderson (1966, p. 42) that deviations caused by violating this requirement are usually small.

3.1.3. *The open end*

The open end contained the fresh water source and an overflow tube or weir to maintain the total depth of the water, H, in the channel. An additional outlet was placed in the bottom of the open section to remove the dense bottom water more effectively. The fresh water source was fed by tap water. The source itself consisted of a box with one side open towards the closed end. The incoming fresh water was calmed by a layer of thick foam-like material before it entered the channel. The supply of fresh water was always kept slightly higher than the actual amount of water flowing through the sill region into the closed end in order to prevent remixing of the dense bottom water with the fresh inflow.

3.2. *Data collection*

3.2.1. *Buoyancy flux and density profiles*

In the present experiment the buoyancy flux, which was applied to the surface, depended both on the volume flow rate and the density of the brine given to the sources. The flow rate $V_{S_i}t^{-1}$ [cm^3 s^{-1}] for each source was determined by measuring the volume of the brine, V_{S_i}, during a certain time period t. This flow rate then was associated with a particular setting on the scale of the flow meter. This setting was kept constant throughout any one experiment to an accuracy of $\pm 2\%$. The density of the brine (ρ_S) was measured using a 100 ml specific gravity bottle. The buoyancy flux B_0 was then determined by

$$B_0 = \frac{\sum V_{S_i}\, g(\rho_S - \rho_0)}{\sum A_i t \rho_0}, \tag{3.1}$$

where ρ_S and ρ_0 are the densities of the brine and the incoming fresh water respectively and A_i is the area covered by one buoyancy source. Density profiles were measured along the channel at various locations and at different depths. A thin tube with holes on opposite sides sucked water from a specified depth through a conductivity probe. By measuring the temperature also a conductivity value corresponding to 25° C was calculated. For the conductivity measurements a device called a SCTpH meter, manufactured by LabComp was used. A computer program was written to relay the data from the SCTpH meter to a Personal Computer where time and location information was added and stored with each sample. Using the calibration function the conductivity data were transformed into density data.

3.3. *Digital particle image velocimetry* (*DPIV*)

Besides density data, velocity profiles were acquired using a DPIV system. The fluid was seeded with small neutrally buoyant Plyolite particles and these were imaged using a PULNiX TM-9701 CCD-camera. Since a two-dimensional flow is assumed the flow field can be evaluated by using a thin light sheet to illuminate the particles in a vertical plane along the centre of the channel. Images were collected in pairs or quadruples at known time intervals. The image data were digitized using a digitizing board, DT3155, manufactured by Data Translation. The acquisition process was controlled

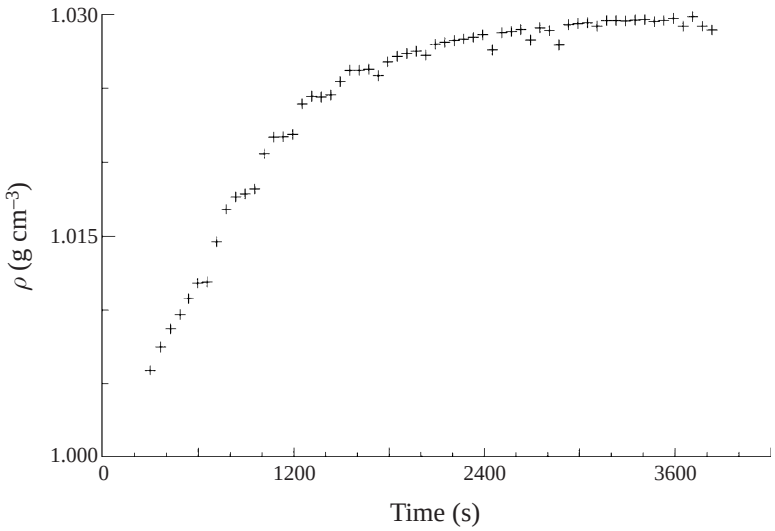

FIGURE 5. Example of the temporal development of the density of the bottom layer after starting the experiment at $t_0 = 0$ s, until the flow reaches steady state (experimental conditions: $W = 4.1$, $\lambda = 57$, $L = 250$ cm, $h = 4.4$ cm, $H = 10$ cm, $B_0 = 0.32$ cm^2 s^{-3}).

by a program especially written and designed for these experiments. The algorithm that was used to evaluate the image data was based on a software development by Fincham & Spedding (1997). Due to the wide range of velocities in any one experiment it was necessary to modify this code by acquiring four images at different time intervals and then, depending on the local fluid velocities, the inner pair of the image quadruple or the outer pair was used to calculate the local flow field. When strong density differences between the inflow and the outflow through the strait region were expected particles of slightly different densities were used simultaneously.

From the density and the velocity data in the sill region a local Froude number was calculated to verify that hydraulic control was established in the contraction region and to identify the location of the supercritical and subcritical regions.

3.4. *Experimental procedure*

For each experiment the whole channel was filled with fresh water to the desired total depth, H. A density probe was placed 1 cm above the bottom near the contraction section, in the closed end of the channel. At time $t = 0$ the buoyancy sources and the fresh water source were turned on. Soon after, a two-layer flow started to develop with inflowing water at the top and outflowing water at the bottom. A steady flow was assumed to exist after there were no significant changes in the density of the bottom layer, for 5 to 10 minutes. Throughout this initial phase of the experiment density data were recorded every minute. It was found that the initial phase lasted at least 60 min. In some cases it could take as long as 100 min, even for a channel as short as 100 cm (see figure 5).

After reaching a steady state density profiles were taken along the channel at intervals of 50 cm. For each profile a series of four to five measurements was conducted at each depth which translated into an averaging time of about 5 min. The spacing in the vertical direction was as small as 1 mm in the proximity of the interface between the upper and lower fluid layers. An example of the density profiles along the channel is shown in figure 6. From these density profiles local values of g' as well

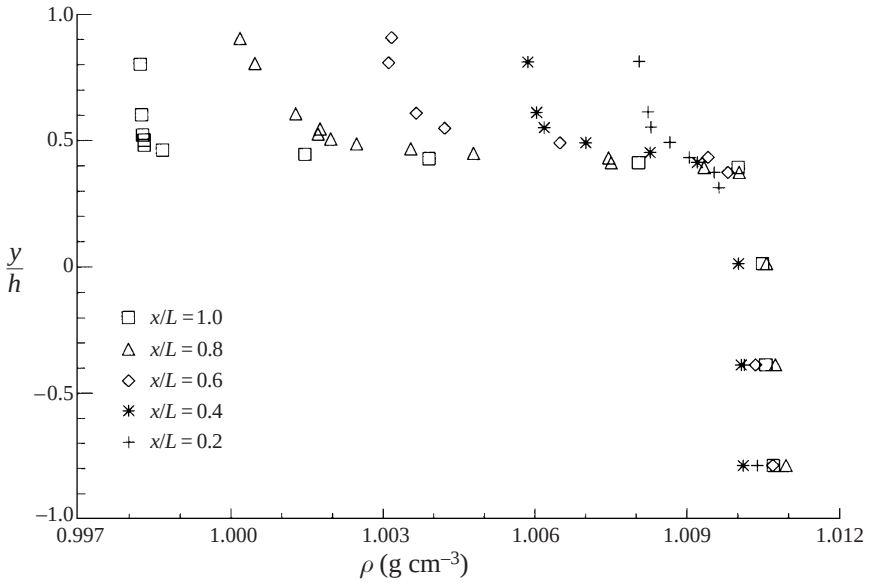

FIGURE 6. Example of the density profiles along the channel (experimental conditions: $W = 1$, $\lambda = 50$, $L = 250\,\text{cm}$, $h = 5\,\text{cm}$, $H = 10\,\text{cm}$, $B_0 = 0.24\,\text{cm}^2\,\text{s}^{-3}$). The density profile at the sill crest is not shown.

as α, β and β_S were deduced. Here $\beta = Y_2 H^{-1}$ is the non-dimensionalized interface depth inside the closed end of the channel with respect to the total depth H, and $\beta_S = (Y_2 - s)h^{-1}$ is the interface depth in the closed end of the channel with respect to the depth h at the sill (see figure 1). The ratio α/β_S is called the drop ratio of the interface from the level in the closed end of the channel to the level at the sill crest made dimensionless by the sill depth h.

After taking the density profiles the velocity profiles were taken in the contraction region. Ten to fifteen groups of image pairs or quadruples were taken about 1 min apart. The flow field was obtained by averaging over the whole time series of images. Velocity profiles were then calculated vertically across the image plane. From the velocity profiles the dimensionless depth, α, of the interface in the contraction region was calculated, based on the velocity profiles. A comparison between the values of α obtained from the velocity profiles and the density profiles show good agreement.

4. Results and discussion

4.1. *Experimental results*

In this section the results of the experiments are discussed. Based on these results the findings will then be applied to a number of natural flow systems. First evidence is sought from the experiments to confirm the basic proportionalities for the scaling of $g'(x)$. Thereafter the scaling is applied to the experimental results without discriminating between the specific control state. Following that, a closer look is taken at the specific control state and the resulting scaling function. For all the reported experiments hydraulic control, i.e. $G^2 = 1$, was established in the contraction/sill area.

The derivations for the scaling of the density difference between the inflowing and the outflowing fluid layers, given by (2.13), (2.14) and (2.18), do not show a difference due to the buoyancy flux B_0. However they do show a difference in the exponents

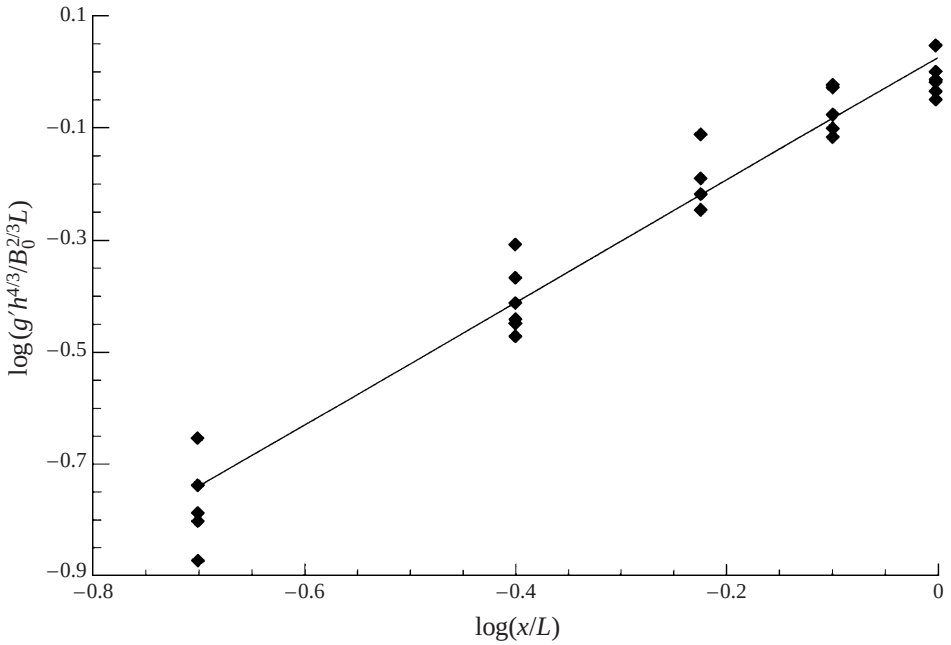

FIGURE 7. Scaling with x/L: $L = 250\,\text{cm}, h = 5\,\text{cm}, H = 10\,\text{cm}$. The regression coefficient has a value of $m = 1.1 \pm 0.05$ which is indicated by the solid line.

of the longitudinal direction x and the depth h. Since the scaling $g'(x) \propto B_0^{2/3}$ must be correct by dimensional arguments as has already been shown by different authors (Phillips 1966; Møller 1984; Brocard *et al.* 1977; and Maxworthy 1994, 1997) we look only at the scaling of $g'(x)$ with x and h in detail.

4.1.1. *Scaling with x*

Figure 7 shows a compilation of experiments with a channel length of $L = 250\,\text{cm}$ and $h = 5\,\text{cm}$ ($\lambda = 50$). The ordinate shows the logarithm of the experimentally measured g' normalized by $h^{4/3}(B_0^{2/3}L)^{-1}$, while the abscissa is $\log(x/L)$. A linear regression analysis reveals a slope of $m = 1.1 \pm 0.05$ which is almost linear and substantially different from the value of $\frac{2}{3}$ suggested by the Phillips (1966) scaling. This finding strongly supports the buoyancy/friction/non-mixing approach of Maxworthy (1997) and the equation (2.18) derived from there.

For all the experiments it should be noted that the density of the bottom layer is constant along the whole length of the channel. Only the density of the top layer increases as fluid parcels move from the strait to the closed end. The observed linear dependence of g' on x, shown in figure 7, confirms the earlier suggestion that there is negligible mixing between the two fluid layers over most of the length of the channel. Only near the closed end of the channel, i.e. over about a distance of the order of H or approximately 5% of the total length, does mixing and overturning occur when a local Richardson number of order unity is reached.

4.1.2. *Scaling with h*

In this subsection we consider the dependence of $g'(x)$ on the depth, h, of the water above the sill crest. Figure 8 shows a set of experiments with a channel length of $L = 250$ cm. The value of h ranges from 2.8 cm to 10.8 cm ($23 \leqslant \lambda \leqslant 89$). Also

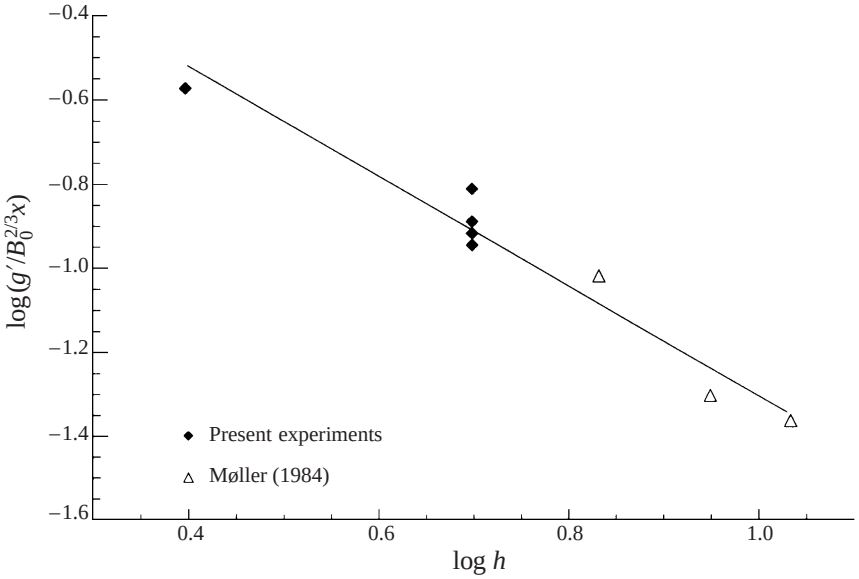

FIGURE 8. Scaling with h: $L = 250\,\text{cm}$. The regression coefficient has a value of $m = -1.3$ which is indicated by the solid line. The value of g' is measured at $x = 150\,\text{cm}$.

included are three experiments by Møller (1984). The ordinate shows the logarithm of g' divided by $(xB_0)^{2/3}$ where the abscissa shows $\log h$. The value of g' used for this plot was taken at a location $x = 150\,\text{cm}$ to avoid effects due to the overturning at the end of the channel which might affect the derivation of the power of h. All these experiments are considered to be of the basic control type. A linear regression analysis yields a regression coefficient of $m = -1.3 \pm 0.06$. This again is close to what is expected $(-\frac{4}{3})$ from the combined friction–hydraulic scaling law.

Based on these findings, a scaling law for $g'(x)$ of the following form is thought to be appropriate:

$$g'(x) \propto \frac{B_0^{2/3} x}{h^{4/3}}. \tag{4.1}$$

4.2. *Hydraulic control states*

In figure 9 we show g' scaled according to the result shown in equation (2.18), i.e. $g'(x) = F(\alpha)\, W^{2/3} \lambda^{-1/3} B_0^{2/3} x/h^{4/3}$ as a function of x/L, for all experiments which were conducted during the course of this work. The length to height ratio covers a range $6.7 < \lambda < 125$, the width ratio varies between $1 \leqslant W \leqslant 8.2$. It can be seen clearly that the scaling linear in x works well for all data. Furthermore note that the experiments in the basic control state ($\diamond$) tend to be slightly above the limiting control (overmixed) experiments ($+$). Since other authors did not state the interface depth α in their works, no comparisons can be made on this point.

The type of the flow control can be determined by the interface depth, α, which is constant ($\alpha = 0.5$) for the limiting control (overmixed) state and variable ($\alpha < 0.5$) for basic control. Figure 10 shows how k depends on α and thus on the type of the flow control. The ordinate shows the value of k evaluated using equation (2.17), which, it will be remembered, was derived from the combination of the internal buoyancy–friction balance and the assumption of a hydraulically controlled flow through the

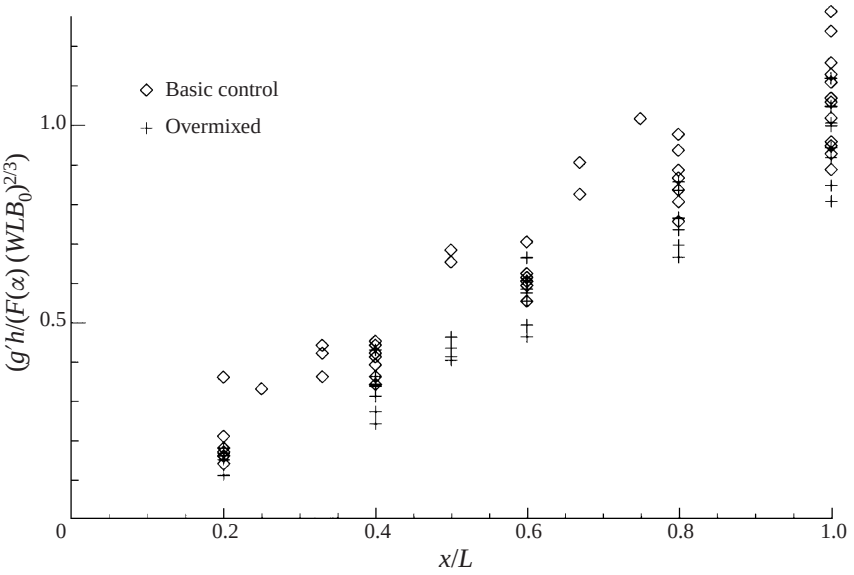

FIGURE 9. Data for all experiments under both the basic control and limiting control (overmixed) state; g' is non-dimensionalized as in (2.18).

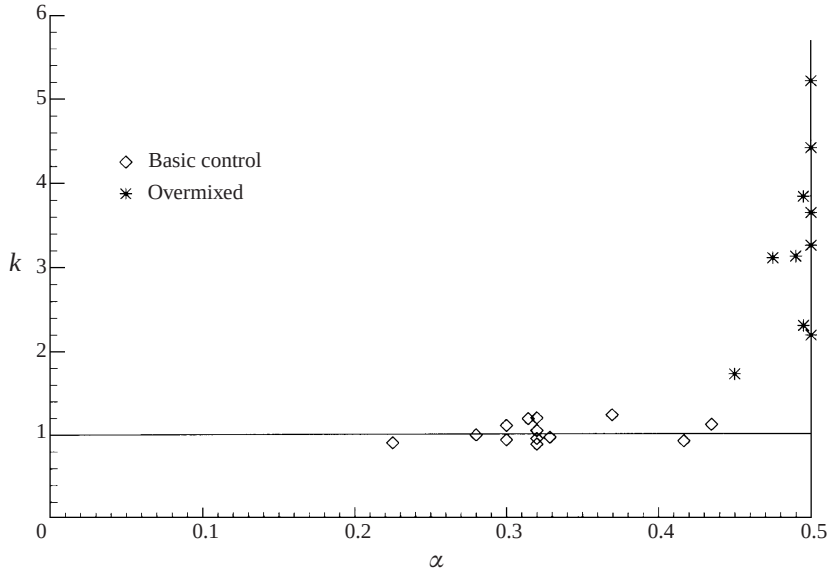

FIGURE 10. The value of k, from equation (2.18), for all experiments under both basic and limiting (overmixed) control, versus α.

contraction. The graph shows that for values of $\alpha < 0.45$, the proportionality factor is constant with $k \approx 1$ representing basic control. When $\alpha \approx 0.5$, k becomes independent of α representing the limiting control (overmixed) state with a proportionality factor $k = 2.52W^{2/3}\lambda^{-1/3}$ (i.e. equation (2.17) evaluated using $F(\alpha = 0.5) = 2.52$). This plot shows the significance of the assumption of a hydraulic control condition in the contraction and the necessity to distinguish between the two possible control

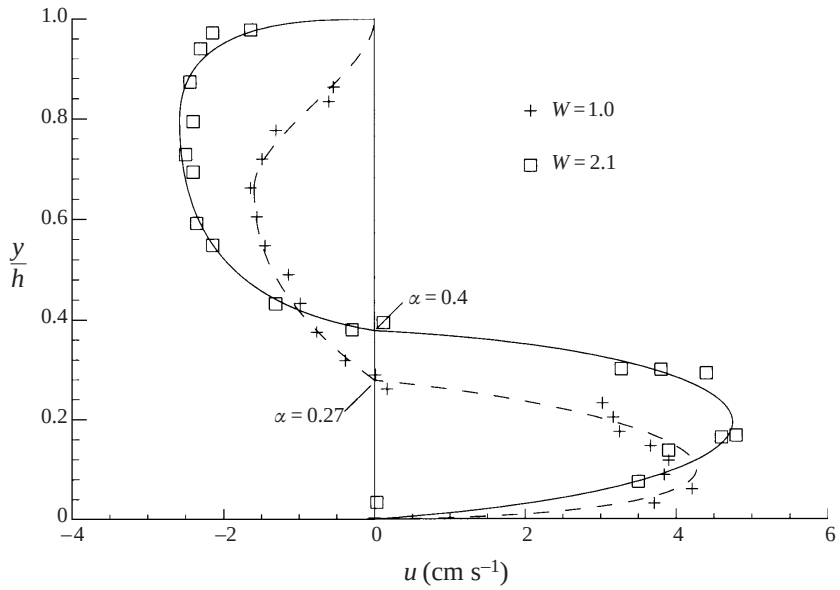

FIGURE 11. Example of the increase in the interface depth, α, from 0.27 to 0.4 when W increases from 1 to 2.1 for a flow in the basic control state. The other applicable parameters for both experiments are: $\lambda = 50$, $L = 250\,\text{cm}$, $h = 5\,\text{cm}$, $H = 10\,\text{cm}$, $B_0 = 0.12\,\text{cm}^2\,\text{s}^{-3}$).

conditions, i.e. basic control and limiting control (overmixed), in order to further investigate the flow.

Also note that, once k is known, the value of $F(\alpha)$ can be derived from the geometry of the channel by solving (2.17) for $F(\alpha)$:

$$F(\alpha) = k\lambda^{1/3} W^{-2/3}. \tag{4.2}$$

Of course this equation is true only as long as its right-hand side is equal to or above the minimum value of $F(\alpha)$, i.e. for the basic control state. However, if the geometry is such that its right-hand side drops to or below the minimum value of $F(\alpha)$, i.e. 2.52, the flow is in the limiting control (overmixed) state and equation (4.2) can be used to determine the critical ratio λ or W, if one of them is fixed, for which the flow reaches the limiting control state. These results show that (2.18) can be used to easily calculate the density difference, or $g'(x)$, if the control state is known. There is a small transition region for $0.45 < \alpha < 0.5$ which is due to the difficulty of exactly determining the interface depth when a rectangularly shaped sill is used. There might also be a slight indeterminacy between the two control states close to the transition between the two states.

The following two subsections are devoted to a more thorough investigation of each of the two flow states basic and limiting control.

4.2.1. *Basic control conditions*

Basic hydraulic control is always achieved with a sill of sufficient height in the contraction area, i.e. when the overflow is isolated from the main basin. For all the reported experiments this requirement was met with a height above the sill $h \leqslant 5\,\text{cm}$ (figure 1*b*). The lower layer beyond the sill in the exit accelerates so that the flow becomes supercritical ($G^2 > 1$). On the other side of the contraction region no supercritical flow conditions exist ($G^2 < 1$) and the flow within the closed

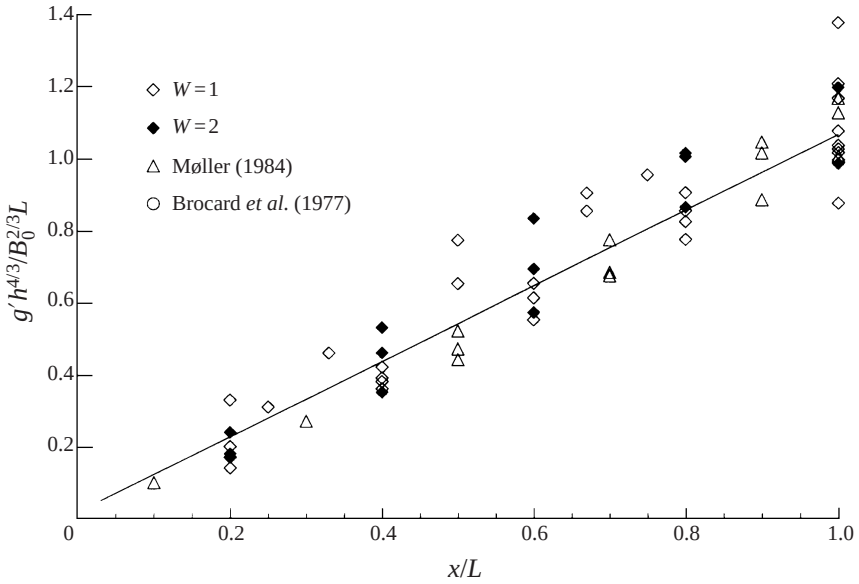

FIGURE 12. Scaling of g' under basic control conditions in the contraction region. Our data sets include experiments with varying width ratios W while for each width ratio L, h and B_0 vary as well ($150 > L > 250$; $2 > h > 5$; $0.11 > B_0 > 0.36$). Additionally data by Møller (1984) and Brocard *et al.* (1977) are shown.

end of the channel is not hydraulically separated from the flow condition in the contraction (figure 1*c*). This feedback between the contraction and the closed end of the channel accounts for k being constant for the basic control case. Depending on the channel geometry W, λ and the buoyancy B_0 applied to the surface area, α adjusts accordingly. This means using (2.17): as W increases, for example, $F(\alpha)$ must decrease and α approaches $\frac{1}{2}$. Using results from the present experiments this effect is revealed in the two velocity profiles of figure 11 where, for otherwise identical conditions, as W increases α increases also.

Figure 12 shows g' made dimensionless by $B_0^{2/3}L/h^{4/3}$ for all experiments performed under basic control conditions including different lateral contraction ratios $1 \leqslant W \leqslant 2$ and different values of λ. Besides our experiments the results of Møller (1984) and Brocard *et al.* (1977) are included. The figure clearly indicates that there is no difference in the scaling law for $g'(x)$ for different values of W or λ. In order not to complicate the figure, the individual values of λ are not indicated separately but they are, in fact, different for each value of W. A linear regression analysis yields a coefficient of $m = 1.04 \pm 0.04$ and is represented by the solid line. The final scaling function for basic control thus takes the form

$$g'_{bc}(x) = (1.04 \pm 0.04)\,\frac{B_0^{2/3}x}{h^{4/3}}. \tag{4.3}$$

For all experiments with basic control the drop ratio, α/β_S, of the interface from the closed end of the channel to the interface depth over the sill crest is $0.64 < \alpha/\beta_S < 0.72$ which is close to $\frac{2}{3}$. This is the same as the theoretical value found for the drop ratio for single-layer flow over a weir, assuming energy conservation (see Henderson 1966). Therefore the basic control case can be viewed as a two-layer flow with the lower layer as the active layer, i.e. with $Fr_1^2 \ll Fr_2^2$. Figure 13 shows an example of the

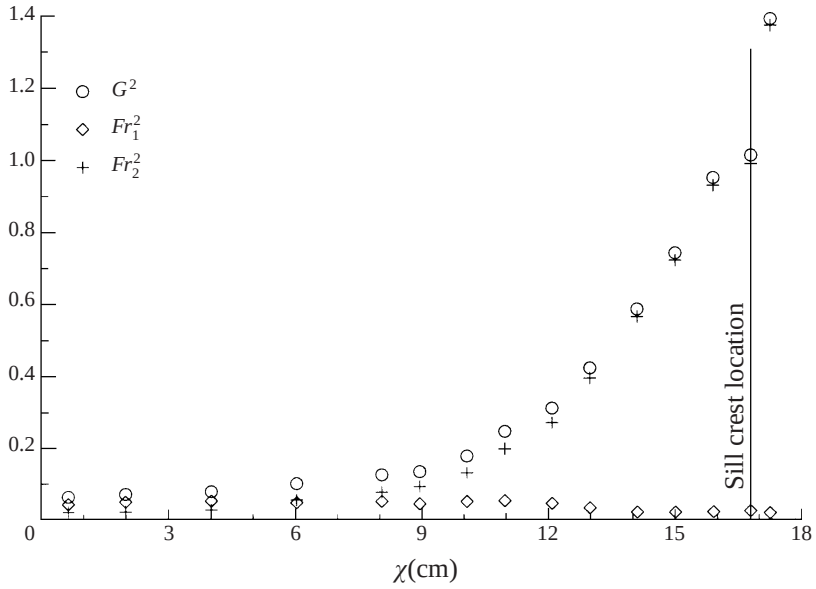

FIGURE 13. An example of the development of the individual Fr_i and the composite Froude number G, for an experiment in the proximity of the sill crest (experimental conditions: $\lambda = 50$, $W = 1$, $B_0 = 0.12\,\mathrm{cm^2\,s^{-3}}$, $L = 250\,\mathrm{cm}$, $h = 5\,\mathrm{cm}$, $H = 10\,\mathrm{cm}$). The position of the sill crest is depicted by the vertical line. The dip in the data across the sill crest is caused by the bar-shaped sill which was used in this experiment. On the horizontal axis a local, arbitrary variable χ is used.

development of the individual Fr_i and G in the proximity of the sill crest which shows that the flow is clearly dominated by the lower fluid layer.

Only for low values of λ (i.e. $\lambda < 20$) does the scaling function show deviations from the suggested scaling, (4.3), with values of k higher than 1.04. This is presumably due to the fact that mixing, in the end region, takes place over a substantial fraction of the channel length in these cases.

For comparison the same data as in figure 12 are shown again in figure 14 based on the Phillips (1966) similarity approach. A linear regression analysis of the data in this case gives a coefficient of $m = 4.1$ which is represented by the solid line in the figure. The line intercepts the x-axis at a value some 17% from the closed end of the channel where the density difference between the two layers according to this model should became zero. This was clearly not observed either in the experiments presented here or in experiments conducted by Møller (1984).

4.2.2. *Limiting control* (*overmixed*) *flow conditions*

Increasing the width ratio, W, and/or the aspect ratio, λ, eventually established a flow under limiting control, i.e. $\alpha = 0.5$. The flow in this case had reached a maximum exchange rate through the contraction. Figure 15 shows the results for the experiments which were conducted in this state. Besides experiments with a sill (solid symbols), those with no sill and a lateral contraction only (open symbols) were conducted. This time a value of $k = 2.52W^{2/3}\lambda^{-1/3}$ was used, which was found to be appropriate for these cases.

A linear regression analysis of the data plotted as $g'h/2.52(WLB_0)^{2/3}$ vs. x/L gives a coefficient of $m = 1.04 \pm 0.05$, which, interestingly, is the same as the value found in the basic control case. Using this corrected value, the final scaling law for the limiting

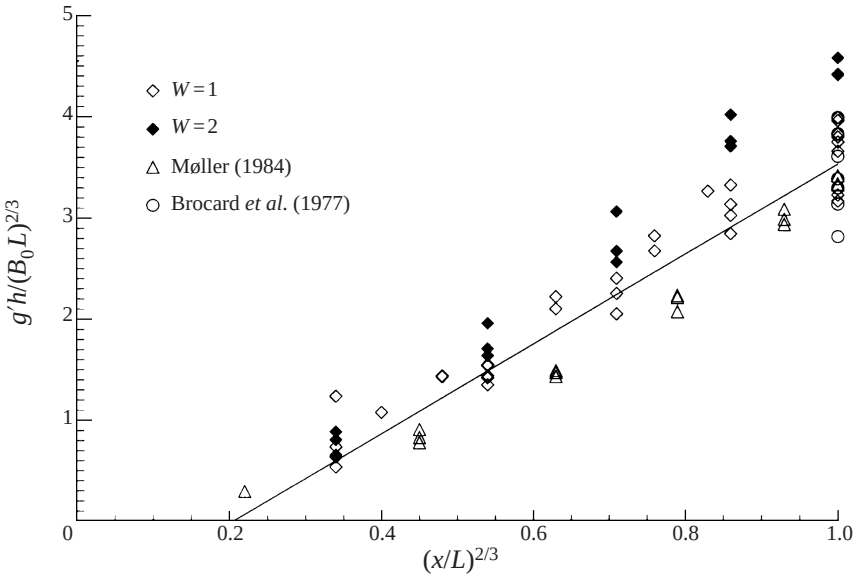

FIGURE 14. As figure 12 but based on the approach of Phillips (1966).

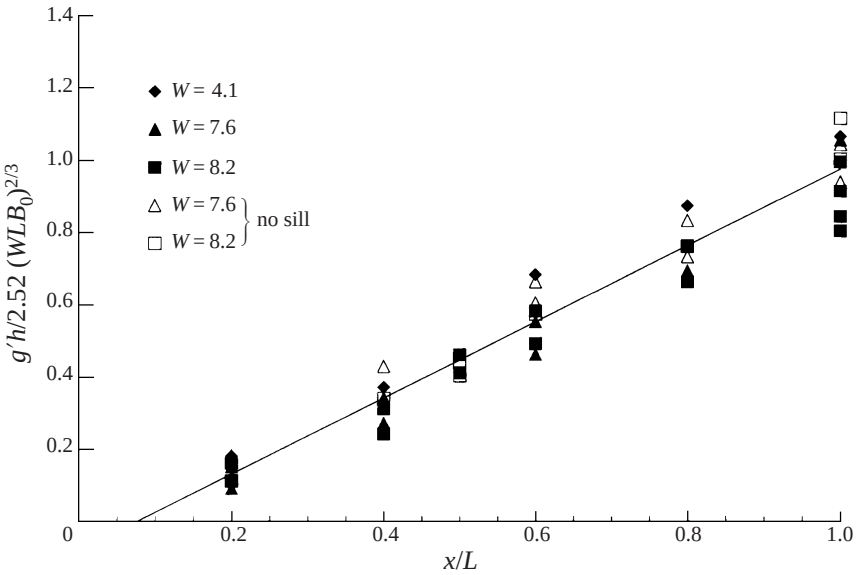

FIGURE 15. Scaling of g' for the limiting control (overmixed) cases. This plot also includes configurations with a lateral contraction only. Solid symbols represent lateral contraction plus sill, and open symbols a lateral contraction only.

control (overmixed) cases reads

$$g'_{lc}(x) = 2.62\, W^{2/3} \left(\frac{h}{L}\right)^{1/3} \frac{B_0^{2/3} x}{h^{4/3}}. \tag{4.4}$$

The line representing the results of the regression analyses intercepts the abscissa at $x/L \approx 0.1$, where the density difference between the two layers vanishes. This

finding is consistent with the experimental observations that the mixing region at the closed end of the channel for the limiting control (overmixed) cases ranges over approximately $0 < x < 0.1L$. No substantial mixing occurs along the rest of the channel. Thus, the general behaviour of the flow is not changed compared with the basic control case. The slightly longer mixing region at the closed end of the channel accounts for the tendency of the limiting control (overmixed) data to be little lower in figure 9 while the slope is the same in both cases. The scaling law (4.4) for the limiting control (overmixed) case should thus include a small constant of about -0.08 with the dimensions of g', or an offset, x_0, of the order of the length of the mixing region. In order to keep the equations as simple as possible, we have not included that correction.

4.2.3. *Summary of experimental results*

Two different conditions of the flow through a contraction region linking fluid reservoirs of different densities have been investigated – basic and limiting control. A scaling law, linear in x, was found to be appropriate to predict the development of the density difference between the two fluid layers along the channel:

$$g'(x) = k\frac{B_0^{2/3}x}{h^{4/3}}. \tag{4.5}$$

A value of $k = F(\alpha)W^{2/3}\lambda^{-1/3}$ was found based on a buoyancy–friction–hydraulic control balance as given in (2.16). The experiments have shown that for the basic control state, due to the feedback between the contraction region and the flow inside the closed end of the channel, k is a constant, with the dynamic property, $F(\alpha)$, adjusting to the geometric conditions. However, if the flow is in the limiting control (overmixed) state this feedback no longer exists and k now depends on the geometric quantities W and λ, while the dynamic part of k, $F(\alpha)$, is constant. Based on the flow conditions and the geometry of the contraction two different expressions for k have been found:

$k_{bc} = 1.04 \pm 0.04$ for basic control $(0.5 > \alpha > 0)$,
$k_{lc} = (2.62 \pm 0.05)W^{2/3}\lambda^{-1/3}$ for limiting control $(\alpha \approx 0.5)$.

4.3. *Applications to natural flow systems*

When natural systems, of the type of interest here, are investigated numerous factors which are not subject to the control of the experimentalist have to be considered. Measurements often represent only snapshots of the whole process or are restricted to a few locations. Estimates of evaporation rates or fluid transport often vary by a factor of two. However, compiling all available information can still give a good framework for the application of experimental results to natural systems.

Two different natural systems have been investigated, the Red and the Mediterranean Seas. Of all of the natural systems the Red Sea is probably the one which is best known and most closely fits the experimental design. Its topography and bathymetry are rather simple and the sea–air interface has more or less uniform features for most of the seasonal cycle with regard to wind stress, heating, cooling and net evaporation. The Mediterranean Sea by contrast represents a very inhomogeneous system.

Despite these differences the type of the hydraulic control is determined and the appropriate scaling function applied to both systems.

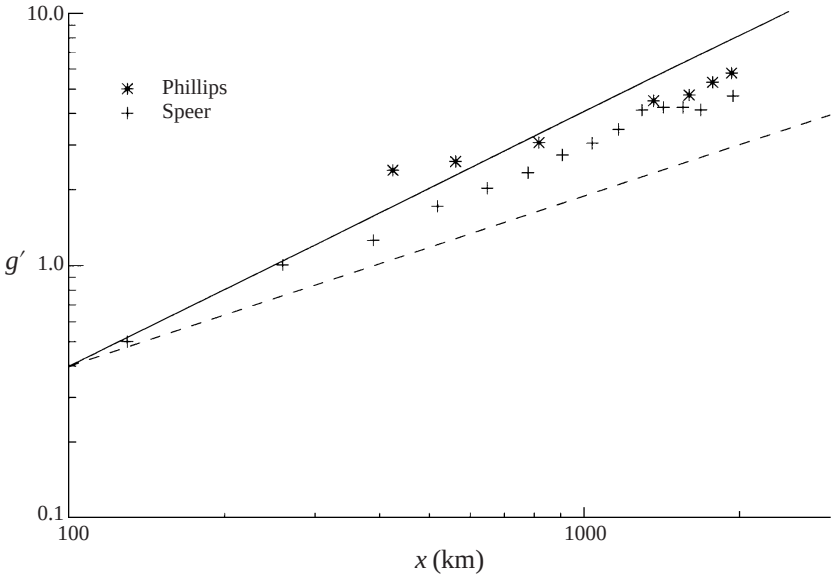

FIGURE 16. The raw data sets of Phillips (1966) and K. Speer (personal communication) for the Red Sea. The solid line represents a linear scaling with x. The dashed line represents a scaling with an exponent of 2/3 in x.

4.3.1. *The Red Sea*

The Red Sea is a natural system which has the closest similarity to the channel of the experiment. Its total length is $L \approx 1960$ km with an average depth and width of 560 m and 200 km respectively. The depth and width of the strait (Bab el Mandab) are 120 m and 20 km respectively. Thus the width ratio is $W \approx 10$. The surface area is estimated to be 460×10^3 km^2. Based on measurements by K. Speer and F. Schott (personal communications) the maximum density difference between the fluid layers of the Red Sea in the exit region is $g' = 4.6\,\mathrm{cm\,s^{-2}}$ and the buoyancy forcing B_0 is variously quoted as $2.0 \times 10^{-4}\,\mathrm{cm^2\,s^{-3}}$ by Garrett *et al.* (1995), $3.4 \times 10^{-4}\,\mathrm{cm^2\,s^{-3}}$ by Grimm (1998), $3.8 \times 10^{-4}\,\mathrm{cm^2\,s^{-3}}$ by Maxworthy (1997) and $4.4 \times 10^{-4}\,\mathrm{cm^2\,s^{-3}}$ by Phillips (1966). Here we will use the value of $3.4 \times 10^{-4}\,\mathrm{cm^2\,s^{-3}}$. The type of flow found at Bab el Mandab is one of basic control. Hydraulic control is established by the pronounced sill and the extensive downsloping of the sea floor towards the Arabian Sea basin, past the Strait. The interface height above the sill crest gives $\alpha \approx 0.26$ (Maxworthy 1997), well within the requirement for the basic control condition. Here x is measured from the southern tip of the Sinai peninsula. No substantial river run-off or precipitation exists within the Red Sea basin.

As a first attempt at data reduction, using values of $g'(L)$, L, h, and B_0 given above, the proportionality constant k, evaluated at the exit from (2.15), is 1.26. This is very close to, within 20%, the value of 1.04 found in the experiments. Using the Phillips (1966) scaling the value becomes 34.3, which is much larger than that found experimentally.

Secondly, if we look at the details of the longitudinal distribution of g' as represented by the K. Speer (personal communication) data in figure 16 (+, January–March flow), a regression coefficient is found of $m = 0.83$. This value is less than a linear development of the density difference between the two fluid layers. Compared with the experiments additional effects have to be considered. Most important are the

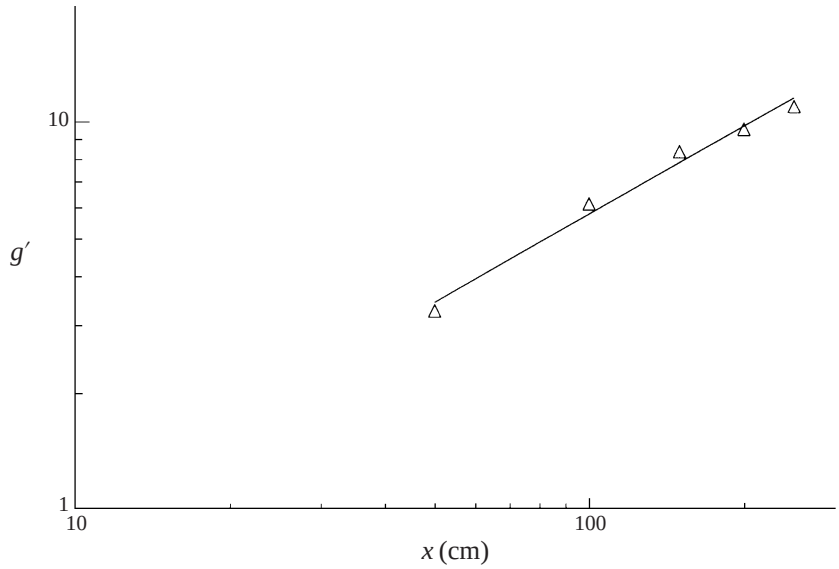

FIGURE 17. Experiment with locally variable B_0 (for $0 < x < 0.4L$: $B_{0_i} = 0.22\,\mathrm{cm^2\ s^{-3}}$; for $0.4L < x < L$: $B_{0_i} = 0.13\,\mathrm{cm^2\ s^{-3}}$). The solid line represents a scaling with an exponent of 0.75 with x (experimental conditions: $L = 250$, $h = 5\,\mathrm{cm}$, $H = 10\,\mathrm{cm}$.)

effects of steady winds blowing along the length of the Red Sea. Throughout most of the year the prevailing winds are from the NNW, opposing the flow direction of the upper fluid layer and thus tending to slow it. Only during the winter do the winds blow in the opposite direction, and therefore with the flow, in the southern part of the Red Sea (Maillard & Soliman 1986). Since the data by K. Speer (personal communication) were acquired during the winter, winds were blowing in the direction of the upper fluid layer in the southern part of the Red Sea while in the North the flow is slowed by opposing surface winds.

The data by Neumann & McGill (1961), used by Phillips (1966), were gathered in early summer. During that time the winds typically blew against the flow direction of the upper fluid layer over the whole surface, accounting for even stronger effects on the resulting flow pattern. Even a three-layer type of flow can occur during summer. Here an upper layer driven by the wind stress with a thickness of about 20–40 m, forms on top with a southerly flow direction, while the inflow from the Arabian Sea takes place in the intermediate layer. The regression coefficient for this data set is $m = 0.59$ with a large non-zero buoyancy jump, at $x = 0$ (figure 18). This value of the slope is close to the value of $\frac{2}{3}$ used by Phillips (1966) to support his scaling function (2.13).

From the experiments and observations discussed above and the remarks on the specific conditions in the Red Sea area, one concludes that the scaling by Phillips (1966) is unlikely to apply for various reasons. First it requires strong vertical mixing over the whole depth of the upper two (three) fluid layers. From our experiments we can find no reason that thorough mixing is possible at the large Richardson numbers that prevail in both the natural and the laboratory systems. However, results from an experiment with a spatially varying buoyancy forcing, $B_0(x)$, show that the overall scaling, $g'(L)$, still applies when the *mean value* of B_0 is employed, even if the local distribution of g' along the channel is not linear (figure 17). The exponent of x for

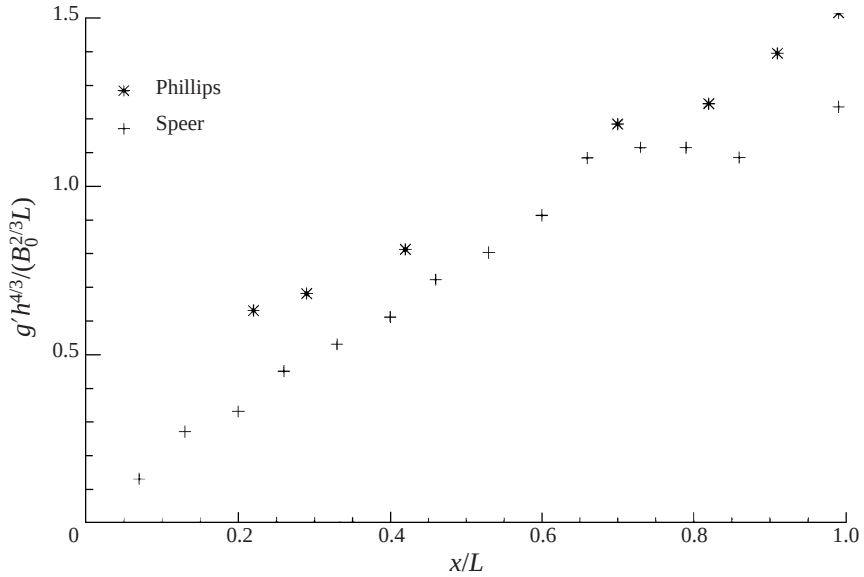

FIGURE 18. Data sets by Phillips and Speer for the Red Sea scaled according to equation (2.18) i.e. assuming basic control.

the case shown is 0.75. Therefore a nonlinearity of $g'(x)$ for the Red Sea can be attributed to other effects than mixing between the layers, i.e. extra cooling or higher evaporation rates in the northern part of the sea, as well as longitudinal variations in the wind stress. Also note that as soon as the strong wind stress, over the whole length of the Red Sea in summer relaxes to the winter pattern, the exponent of x shifts closer to unity.

As a result it is useful to derive the proportionality factor, k, for the Red Sea, for both data sets and compare the resulting values for the Phillips (1966) and the frictional approach with the experimental results. Figure 18 shows the Red Sea data plotted the same way as the experimental data for the basic control conditions of figure 12. From this plot the factor k can be computed for both data sets. Values of $k = 1.14$ and 1.23 are found for the data sets by Neumann & McGill (1961) and K. Speer (personal communication) respectively. The values are fairly close to the value which is to be expected for a 'clean', non-mixing two-layer flow. Despite the fact that complicating effects do occur in the Red Sea, the hydraulic constraint at the sill governs the scaling of g' according to equation (4.3) and the results compare well with the experiments.

On the other hand, using the similarity approach of Phillips (1966) to scale the density difference a value of $k \approx 37$ is obtained which is some 10 times higher than the value found from the experiments (see figure 14).

4.3.2. *The Mediterranean Sea*

The other natural system to be considered is the Mediterranean Sea. The very narrow and shallow Strait of Gibraltar separates it from the Atlantic Ocean. The narrowest section (Tarifa section) is only 12 km wide and the shallowest section (Camarinal Sill) has a maximum depth of 350 m. The cross-section is almost a triangular shape for which an effective or equivalent rectangular sill depth of

$h = 200\,\mathrm{m}$ is assumed (see below). The total length of the Mediterranean is $L = 3750\,\mathrm{km}$ with a surface area of $2.5 \times 10^{12}\,\mathrm{m}^2$ which gives an average width (W_b) of 670 km. The width ratio is then $W = 56$. Based on measurements by Farmer & Armi (1988) $g'(L) = 2.5\,\mathrm{cm\,s^{-2}}$ and $B_0 = 1.6 \times 10^{-4}\mathrm{cm^2\,s^{-3}}$. There is an ongoing debate as to whether the Mediterranean Sea is under limiting control (overmixed), or not. Due to the pronounced sill the Mediterranean Sea clearly is hydraulically controlled and complex hydraulic flows have been observed (Farmer & Armi 1988). Garrett, Bormans & Thompson (1990) suggest that the Mediterranean is under limiting control (overmixed) during the first half of the year and under basic control for the second half of the year.

Due to strong barotropic tidal forcing the hydraulic flow at the Strait of Gibraltar is never steady. However one can treat the region as a 'black box' which generates some average condition within the partially enclosed sea, i.e. all the nonlinear exchange effects can be averaged out to give an effective control condition at the strait. Of course this is only possible since the time constant for a change in the sea is so long that it cannot respond instantaneously to the changes in the control condition and because the internal waves that carry information about the control attenuate rapidly as they leave the region of the strait. For this averaged condition based on the parameter values given above, a value of $k = 1.23$ is calculated from (2.15). Assuming basic control conditions, this value should read 1.04. Based on limiting control conditions a value of $k = 1.39$ is predicted from (4.4). Thus the value calculated from the field measurements lies between the predictions for the two different averaged control conditions $1.04 < k < 1.39$ both of which seem to occur over the period of a year. The assumption of an effective depth of $h = 200\,\mathrm{m}$ comes from the thought that it is appropriate to keep the actual triangular cross-sectional area of the strait the same as the effective cross-section of an equivalent rectangular shape, though no experiments seem to exist to verify this assumption. Altering h between $175 \leqslant h \leqslant 225\,\mathrm{m}$ shifts k closer to either the basic control or the limiting control (overmixed) condition. This finding again supports the contention that the overall scaling of $g'(L)$ depends mainly on the control state of the flow at the sill.

4.3.3. *Summary for natural systems*

Two different natural systems have been investigated. It has been shown that the different flow types investigated in the experiments can be applied to them. In order to apply a scaling model it is necessary to know exactly the exit flow condition that is appropriate for the specific system.

For the Mediterranean Sea the predicted values of k, from the field measurements, are very close to those from the experiments and between the two states that are thought to exist for the Mediterranean Sea over the annual cycle. Even though this system is very inhomogeneous, interestingly the effective control condition is very close to that found in the experimental system.

For the Red Sea extraneous effects seem to disturb the system to an extent that the application of the experimental results is not straightforward and additional experiments need to be conducted to fully understand the buoyancy distribution in this system. However the application of the experimental results to the Red Sea is already very good in an averaged sense, when one thinks of the possible effects of wind stress and non-uniform buoyancy flux to the upper fluid layer, for example. The values of k (1.14 and 1.23), calculated from the observations, deviate less than 20% from the value predicted from our experimental results.

4.4. *Summary*

It has been shown that a function that is linear in x scales the development of the density difference in exchange flows through straits connected to convectively driven seas. This function can be obtained by a friction–buoyancy balance in the main body of fluid in a long channel, for example. Application of an hydraulic control condition at a strait or contraction region poses a further constraint on the exchange flow. This constraint can then be used to derive a scaling factor k that depends upon the geometrical aspect ratios of the channel (W and λ) and the dynamic properties of the hydraulic flow at the sill/contraction as represented by the function $F(\alpha)$. By using knowledge of the specific control state of the flow, i.e. whether it is under limiting or basic control the value of k can be determined easily.

Comparisons with natural systems have yielded promising results. However it is still necessary to work towards a better understanding of the effects on buoyancy distribution caused by wind stress, complex topography and spatially and temporally non-uniform buoyancy forcing. Experiments need to be conducted to see how details of the strait geometry influence the effective interface height at the strait and how the overall control at a strait is effected when the shallowest and narrowest section do not coincide, etc. Other interesting aspects concern the effect of local sources of dense water connected to the main channel, e.g. the Gulf of Suez or the Gulf of Aquaba in the case of the Red Sea. Finally, work needs to be done in an apparatus which allows higher contraction ratios, W, than were used during this work to model even more closely the Red Sea ($W \approx 10$) and the Mediterranean Sea ($W \approx 56$).

We would like to acknowledge the German Academic Exchange Service for supporting this work over the course of its first two years. Also, we would like to thank the Office of Naval Research, contract N00014-97-1-0671, for additional funding of the project.

REFERENCES

Armi, L. 1986 The hydraulics of two flowing layers with different densities. *J. Fluid Mech.* **163**, 27–58.

Armi, L. & Farmer, D. M. 1986 Maximal two-layer exchange through a contraction with barotropic net flow. *J Fluid Mech.* **164**, 27–51.

Brocard, D. N., Jirka, G. H. & Harleman, D. R. F. 1977 A model for the convective circulation in sidearms of cooling lakes. *Ralph M. Parsons Laboratory for Water Resources and Hydrodynamics, Mass. Inst. of Technology, Rep.* 223.

Farmer, D. M. & Armi, L. 1986 Maximal two-layer exchange over a sill and through the combination of a sill and contraction with barotropic flow. *J. Fluid Mech.* **164**, 53–76.

Farmer, D. M. & Armi, L. 1988 The flow of Atlantic water through the Strait of Gibraltar. *Prog. Oceanogr.* **21**, 1–105.

Fincham, A. & Spedding, G. 1997 Low cost, high resolution DPIV for measurements of turbulent fluid flow. *Exps. Fluids* **23**, 449–492.

Garrett, C., Bormans, M. & Thompson, K. 1990 Is the exchange through the Strait of Gibraltar maximal or submaximal? In *The Physical Oceanography of Sea Straits* (ed. L. J. Pratt), pp. 271–294. Kluwer.

Garrett, C., Speer, K. & Tragou, E. 1995 The relationship between water mass formation and the surface buoyancy flux, with application to Phillips Red Sea model. *J. Phys. Oceanogr.* **25**, 1696–705.

Grimm, T. 1998 Dichteinduzierte Strömungen in einem langen Kanal. PhD thesis, Max Planck Institut für Strömungsforschung, Bunsenstr. 10, D-37073 Göttingen, Germany.

Grimm, T. & Maxworthy, T. 1996 Convectively induced meanflow in a long channel. In *Proc. Ocean Sci. Meeting*. American Geophysical Union.

HENDERSON, F. M. 1966 *Open Channel Flow*. Macmillan.

LAWRENCE, G. A. 1990 On the hydraulics of Boussinesq and non-Boussinesq two-layer flows. *J. Fluid Mech.* **215**, 457–480.

MAILLARD, C. & SOLIMAN, G. 1986 Hydrography of the Red Sea and exchange with the Indian Ocean in summer. *Oceanologica Acta* **9**, 3.

MAXWORTHY, T. 1994 Mixing in partially-enclosed seas. *Ocean Modelling* **105**, 9–11.

MAXWORTHY, T. 1997 Frictionally and hydraulically constrained model of the convectively-driven meanflow in partially-enclosed seas. *Deep-Sea Res.* **44**, 1339–1354.

MAXWORTHY, T. & MONISMITH, S. 1988 Differential mixing in a stratified fluid. *J. Fluid Mech.* **189**, 571–598.

MØLLER, J. S. 1984 Hydrodynamics of an Arctic fjord, field study, Affarlikassaa, West Greenland. PhD thesis, Inst. Hydrodyn. Hydraulic Eng., University Denmark, Lyngby.

NEUMANN, A. C. & MCGILL, D. A. 1961 Circulation in the Red Sea in early summer. *Deep-Sea Res.* **8**, 223–235.

PHILLIPS, O. M. 1966 On turbulent convection currents and the circulation of the Red Sea in early summer. *Deep-Sea Res.* **13**, 1146–1160.

STOMMEL, H. & FARMER, H. G. 1953 Control of salinity in an estuary by a transition. *J. Mar. Res.* **12**, 13–20.

TRAGOU, E. & GARRETT, C. 1995 The stratification and circulation of the buoyancy-driven Red Sea. *Ocean Modelling* **110**, 6–9.

WILLIAMS, R. & ARMI, L. 1991 Two-layer hydraulics with comparable internal wave speeds. *J. Fluid Mech.* **230**, 667–691.